Journal of Zhejiang University-SCIENCE C (Computers & Electronics)
ISSN 1869-1951 (Print); ISSN 1869-196X (Online)
www.zju.edu.cn/jzus; www.springerlink.com
E-mail: jzus@zju.edu.cn

Effect of orbital errors on the geosynchronous circular synthetic aperture radar imaging and interferometric processing*

Lei-lei KOU†[1,2], Xiao-qing WANG[1], Mao-sheng XIANG[1], Jin-song CHONG[1], Min-hui ZHU[1]

([1]*National Key Laboratory of Microwave Imaging Technology, Institute of Electronics, Beijing 100190, China*)

([2]*Graduate University of Chinese Academy of Sciences, Beijing 100190, China*)

†E-mail: cassie320@163.com

Received May 26, 2010; Revision accepted Nov. 11, 2010; Crosschecked Feb. 28, 2011

Abstract: The geosynchronous circular synthetic aperture radar (GEOCSAR) is an innovative SAR system, which can produce high resolution three-dimensional (3D) images and has the potential to provide 3D deformation measurement. With an orbit altitude of approximately 36 000 km, the orbit motion and orbit disturbance effects of GEOCSAR behave differently from those of the conventional spaceborne SAR. In this paper, we analyze the effects of orbit errors on GEOCSAR imaging and interferometric processing. First, we present the GEOCSAR imaging geometry and the orbit errors model based on perturbation analysis. Then, we give the GEOCSAR signal formulation based on imaging geometry, and analyze the effect of the orbit error on the output focused signal. By interferometric processing on the 3D reconstructed images, the relationship between satellite orbit errors and the interferometric phase is deduced. Simulations demonstrate the effects of orbit errors on the GEOCSAR images, interferograms, and the deformations. The conclusions are that the required relative accuracy of orbit estimation should be at centimeter level for GEOCSAR imaging at L-band, and that millimeter-scale accuracy is needed for GEOCSAR interferometric processing.

Key words: Geosynchronous circular synthetic aperture radar (GEOCSAR), Orbit error, Imaging, Interferometric processing
doi:10.1631/jzus.C1000170 **Document code:** A **CLC number:** TN957.52

1 Introduction

It is well known that spaceborne synthetic aperture radar (SAR) can offer all-day and all-weather two-dimensional (2D) images of large areas. For spaceborne SAR imaging processing, the quality of SAR images is closely connected with the motion of the satellite platform (Li *et al*., 1985; Zhang and Cao, 2004; Zhou *et al*., 2007). The orbit errors caused by disturbance of satellite affect the Doppler parameters, and then influence the final SAR products (Li *et al*., 1985). In previous research, the effects of orbit perturbation and attitude errors on the conventional 2D spaceborne SAR imaging were analyzed via Doppler parameters. The influence of the satellite orbit error on the radar interferometric phase was studied based on the principle of differential interferometric SAR (DInSAR) (Hanssen, 2002; Zhang *et al*., 2007). The conclusions are that the orbit disturbance is a key factor influencing the quality of SAR products.

A geosynchronous SAR (GEOSAR) concept has previously been presented by Tomiyasu (1978; 1983). The synthetic aperture is obtained with an apparent motion of the geosynchronous satellite induced by non-zero inclination and eccentricity of the orbit. With an about 36 000 km altitude, the GEOSAR can offer a coverage as wide as over 1000 km, and offer the daily or even shorter revisit period of the interested area (Madsen *et al*., 2002; Bruno *et al*., 2006). In previous research, the inclined geosynchronous orbit was chosen to offer the linear track, so the SAR can work as the traditional sidelook strip mapping SAR (Tomiyasu, 1983; Madsen *et al*., 2001). In fact, the geosynchronous orbit can offer a much more flexible subsatellite track than a low earth orbit, such

* Project (No. 2009CB724003) supported by the National Basic Research Program (973) of China

as circle, ellipse, 8-like, and some other complex tracks (Erik, 1994; Cazzani *et al*., 2000). Thus, the circular SAR can be realized on the geosynchronous orbit if the subsatellite track is designed to be a circle. The geosynchronous SAR with a circular subsatellite track is called geosynchronous circular SAR (GEOCSAR) in this paper. The circular subsatellite track can provide true 3D images with improved ground resolution, and a geosynchronous satellite will provide a steady and appropriate platform for circular SAR (Axelsson, 2004; Colesanti and Perissin, 2006; Cantalloube *et al*., 2007). Besides, the coverage region can be mapped from different view directions, and a GEOCSAR can provide the 3D displacement data by repeat pass interferometry (Madsen *et al*., 2001; NASA, 2003).

Similar to the conventional spaceborne SAR, the determination of the GEOCSAR orbit accuracy is important, based on the analysis of the effects of orbit disturbance on the SAR products. For geosynchronous satellites, the motion of the satellites is more complex, and the orbit is influenced mainly by perturbation causes such as anisotropic geopotential, lunisolar attraction, and solar radiation pressure (Shrivastava, 1978; Erik, 1994; Yoon *et al*., 2004). The orbit perturbations lead to the variation of geosynchronous orbit elements, and then the regular motion of GEOCSAR becomes disturbed. Thus, the satellite motion can be described as the contributions of perturbations and the difference of designed orbit parameters and the geostationary orbit. The orbit estimation should consider both the perturbations and the designed orbit parameters. Based on the model of perturbations, the orbit can be estimated using the ground control points (GCPs) method or other measuring techniques, and the orbit errors depend on the difference between the real orbit and the estimated values. In this paper, the effects of orbit errors on the performances of GEOCSAR images, interferograms, and the corresponding surface deformations are analyzed, according to the basic principle of imaging and interferometric processing. From interferometric processing of three subapertures or more, the 3D surface deformation can be gained, which is a remarkable advantage of GEOCSAR. The effects of orbit errors on deformations in three dimensions are compared and analyzed as well. The analyses and simulations quantify and verify the required accuracies of GEOCSAR orbit estimation.

2 GEOCSAR system geometry

According to the Kepler differential equation, when the eccentricity (e) and inclination (i) are small, the satellite position equation can be expressed as (Erik, 1994; Cazzani *et al*., 2000)

$$\begin{cases} \lambda \approx 2e\sin\left(\omega(\tau-\tau_{\mathrm{p}})\right)+\Omega+\lambda_0, \\ \phi \approx i\sin\left(\omega(\tau-\tau_{\mathrm{p}})+\Omega\right), \\ r \approx A\left(1-e\cos\left(\omega(\tau-\tau_{\mathrm{p}})\right)\right), \end{cases} \tag{1}$$

where τ_{p} is the time at which the satellite passes through the perigee position, λ and φ are the longitude and latitude of satellite nadir respectively, λ_0 is the ascending node longitude, Ω is the argument of perigee of the orbit, ω is the earth rotation angular velocity, r is the geocenter distance of the satellite, and A=42 164.2 km is the major semi-axis of the orbit.

Consider the geometry shown in Fig. 1. The reference system is the earth body fixed coordinates centered at the geocenter, with X axis pointing to the North Pole, Z axis pointing to the nominal geostationary point of the satellite, and Y direction normal to the XZ plane. Then the satellite position can be represented as

$$\begin{cases} X \approx r\phi \approx Ai\sin\left(\omega(\tau-\tau_{\mathrm{p}})+\Omega\right), \\ Y \approx r(\lambda-\Omega-\lambda_0) \approx 2Ae\sin\left(\omega(\tau-\tau_{\mathrm{p}})\right), \\ Z=\sqrt{r^2-X^2-Y^2}. \end{cases} \tag{2}$$

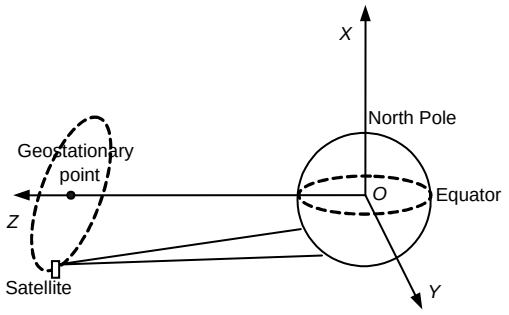

Fig. 1 Coordinates and the satellite motion relative to the geostationary point

Letting $\theta=\omega_\tau(\tau-\tau_{\mathrm{p}})$, which is within $[-\pi, \pi)$ during a satellite period, and assuming Ω=90°, i=2e, the projection of the satellite trajectory on the XY plane would be a circle with radius $R_{\mathrm{g}}=Ai$:

$$\begin{cases} X \approx Ai\sin(\Omega+\theta) = R_{\mathrm{g}}\cos\theta, \\ Y \approx 2Ae\sin\theta = R_{\mathrm{g}}\sin\theta, \\ Z = \sqrt{(A-Ae\cos\theta)^2 - X^2 - Y^2} \\ \quad \approx H - 0.5Ae\cos\theta = H - 0.5R_{\mathrm{g}}\cos\theta, \end{cases} \tag{3}$$

where H=A. The argument of perigee can also be 270°, and then X=−R_{g}cosθ in Eq. (3). We use Ω=90° in the following derivations. It can be seen from Eq. (3) that the SAR path projected to the XY plane is circular, and GEOCSAR imaging mode is produced. When the inclination i is still small and $\Omega\neq$90°, $i\neq 2e$, an elliptical subsatellite ground track may be produced. With a large orbit inclination angle i, 20° for example, the subsatellite track will be presented as 8-like.

In the 3D space, the GEOCSAR path of Eq. (3) is actually an ellipse, whereas the SAR on this trajectory can also obtain high resolution 3D imaging as the standard circular SAR. Besides, GEOCSAR can produce the high resolution 3D surface deformation measurement by repeat pass interferometry because of its multiple azimuthal observations.

3 Geosynchronous orbit errors

3.1 Geosynchronous orbital elements

For the geosynchronous orbit, the geosynchronous orbital elements are usually used when $\|\boldsymbol{i}\|$<<1, $\|\boldsymbol{e}\|$<<1:

$$(A, \lambda_{\mathrm{e}}, e_x, e_y, i_x, i_y) = (A, \lambda_{\mathrm{e}}, \boldsymbol{e}, \boldsymbol{i}), \tag{4}$$

where $\boldsymbol{i}$=(i_x, i_y) is a 2D vector of the inclined angle, $\boldsymbol{e}$=(e_x, e_y) is a 2D vector of eccentricity, and λ_{e}=λ_0+Ω is the relative average longitude.

The geosynchronous orbit is determined by the geosynchronous orbital elements, which are influenced by the orbital perturbations. For GEOCSAR imaging, the time of synthetic aperture is one day or less. Hence, the orbit is affected mainly by the short-period perturbations. The size of the satellite motion due to the perturbations depends on the source of the perturbations. Concretely, the geosynchronous orbital elements will be modified mainly by the zonal and tesseral terms of the Earth's gravity and the lunisolar perturbations (Musen and Bailie, 1962; Shrivastava, 1978; Erik, 1994).

3.2 Model of orbit errors

Geosynchronous satellites exhibit resonance characteristics resulting from various harmonics of the geopotential. The general expression of the Earth's potential is (Cassara, 1963)

$$U = -\frac{\mu_{\mathrm{e}}}{r}\left\{1 - \sum_{n=2}^{\infty}\left(\frac{R_{\mathrm{e}}}{r}\right)^n \left[J_n P_n(\sin\varphi) - \sum_{m=1}^{n} J_{nm} P_{nm}(\sin\varphi)\cos\left(m(\lambda-\lambda_{nm})\right)\right]\right\}, \tag{5}$$

where μ_{e} is the earth gravitational constant, r, λ, and φ are the geocentric distance, longitude, and latitude respectively, R_{e} is the mean equatorial radius of the earth, P_{nm} is the associated Legendre polynomial, J_n is the zonal term, and J_{nm} is the tesseral term. More fully, P_{nm} is defined by (Cassara, 1963)

$$P_{nm}(z) = (1-z^2)^{m/2}\frac{\mathrm{d}^m}{\mathrm{d}z^m}P_n(z), \tag{6}$$

where P_n is Legrendre's polynomial and z=sinφ.

For geosynchronous orbits of small inclination and eccentricity, the previous research (Kimura and Todo, 1997; Yoon *et al.*, 2004) has concluded that harmonics coefficient J_{22} may contribute most to the tangential perturbing force. The terms of n≤6, m≤6 in the gravitational potential of Eq. (5) are sufficient for practical needs (Shrivastava, 1978).

The presence of the Moon and the Sun results in significant perturbations of geosynchronous satellites. The gravitational attraction of the Sun and the Moon satisfies the same inverse-square law as the attraction of the Earth. According to the astronomical data, the perturbations of the Sun and the Moon are on the same level as that of geopotential effects (Musen and Bailie, 1962; Cassara, 1963; Erik, 1994).

Fig. 2 (Erik, 1994) shows plots of the short-term variation models of the satellite position and osculating orbital elements for spring tide. The perturbing effect in this time is the strongest. The perturbations from the zonal and tesseral terms of the Earth's gravity and from the lunisolar attraction are included in the orbital motion (Fig. 2), including the satellite distance from the Earth, r, the semimajor axis A, the average longitude λ_{e}, and the two eccentricity vector components e_x and e_y.

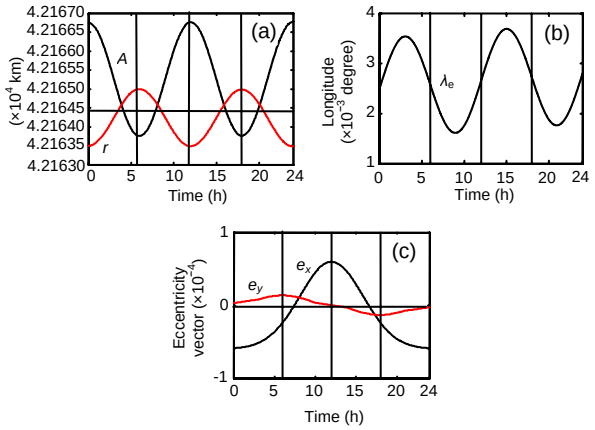

Fig. 2 Short-term variation of the satellite distance from the Earth, *r*, the semimajor axis *A* (a), the average longitude λ_e (b), and the two eccentricity vector components e_x and e_y (c) during a spring tide (Erik, 1994)

Fig. 2a shows that the highest perturbing effect in *r* is about 2.2 km. Fig. 2b shows the variation of the longitude λ_e with an amplitude of 0.0008°, which implies an about 3.0 km highest variation in the along-track position ($X=A\lambda_e\approx 3$ km). From Eq. (5) and Fig. 2, we can see that with the short-term perturbing effects, the geosynchronous orbital elements will vary in the form of

$$\begin{cases} A = A_0 + \sum_{n=1}^{\infty} \delta A_n \cos(n\theta + \varphi_n), \\ \lambda_e = \lambda_{e0} + \sum_{n=1}^{\infty} \delta\lambda_{en} \cos(n\theta + \phi_n), \\ e = |\boldsymbol{e}| = e_0 + \sum_{n=1}^{\infty} \delta e_n \cos(n\theta + \psi_n), \\ i = |\boldsymbol{i}| = i_0 + \sum_{n=1}^{\infty} \delta i_n \cos(n\theta + \xi_n), \end{cases} \tag{7}$$

where A_0, λ_{e0}, e_0, and i_0 are constant orbital elements, and δA_n, $\delta\lambda_{en}$, δe_n, and δi_n are the *n*th terms of the perturbation coefficients, φ_n, ϕ_n, ψ_n, and ξ_n are the *n*th terms of the phases. The major contributing terms are $\delta A_2\cos(2\theta+\varphi_2)$, $\delta\lambda_{e2}\cos(2\theta+\phi_2)$, $\delta e_1\cos(\theta+\psi_1)$, and $\delta i_2\cos(2\theta+\xi_2)$. For orbit measurement, the constant terms and the major orbital element terms caused by perturbations will be estimated with the method of ground control points (GCPs) or other measuring techniques (Kimura and Todo, 1997; Ren *et al*., 2003; Liu *et al*., 2006). Hence, the errors of geosynchronous orbital elements are composed mainly of the cosine terms except the major contributing terms that have been accurately measured, i.e.,

$$\begin{cases} \Delta A = \delta A_1\cos(\theta+\varphi_1) + \delta(\delta A_2)\cos(2\theta+\varphi_2) \\ \qquad + \sum_{n=3}^{\infty}\delta A_n\cos(n\theta+\varphi_n), \\ \Delta\lambda_e = \delta\lambda_{e1}\cos(\theta+\phi_1) + \delta(\delta\lambda_{e2})\cos(2\theta+\phi_2) \\ \qquad + \sum_{n=3}^{\infty}\delta\lambda_{en}\cos(n\theta+\phi_n), \\ \Delta e = \delta(\delta e_1)\cos(\theta+\psi_1) + \sum_{n=2}^{\infty}\delta e_n\cos(n\theta+\psi_n), \\ \Delta i = \delta i_1\cos(\theta+\xi_1) + \delta(\delta i_2)\cos(2\theta+\xi_2) \\ \qquad + \sum_{n=3}^{\infty}\delta i_n\cos(n\theta+\xi_n), \end{cases} \tag{8}$$

where ΔA, $\Delta\lambda_e$, Δe, and Δi represent the errors of the orbital elements, $\delta(\delta A_2)$, $\delta(\delta\lambda_{e2})$, $\delta(\delta e_1)$, and $\delta(\delta i_2)$ denote the residual major contributing orbital elements after precise orbit estimation. For gaining more precise orbital elements, the secondary major contributing terms may also be estimated. Therefore, the orbit error in fact depends mainly on the accuracy of orbit estimation using the GCPs method or other measuring techniques. By insertion of the orbital elements into Eq. (3) and making some simple mathematical calculations, we can obtain

$$\begin{cases} \Delta X \approx Ai\cos\theta - (A-\Delta A)(i-\Delta i)\cos\theta \\ \qquad = (A\cdot\Delta i + \Delta A\cdot i - \Delta A\cdot\Delta i)\cos\theta, \\ \Delta Y \approx 2Ae\sin\theta - 2(A-\Delta A)(e-\Delta e)\sin\theta + A\cdot\Delta\lambda_e \\ \qquad = 2(A\cdot\Delta e + \Delta A\cdot e - \Delta A\cdot\Delta e)\sin\theta + A\cdot\Delta\lambda_e, \\ \Delta Z \approx (A - Ae\cos\theta) - (A-\Delta A) + (A-\Delta A)(e-\Delta e)\cos\theta \\ \qquad = \Delta A - (A\cdot\Delta e + \Delta A\cdot e - \Delta A\cdot\Delta e)\cos\theta, \end{cases} \tag{9}$$

where $A-\Delta A$, $i-\Delta i$, and $e-\Delta e$ are the orbital elements after precise estimation using the method of GCPs or a priori orbital information. Inserting Eq. (8) into Eq. (9), it is seen that the orbit errors in (*X*, *Y*, *Z*) coordinates are complex expressions composed of a sum of a series of cosine functions with different amplitudes, periods, and phases.

4 Effects of orbit errors on GEOCSAR images and interferometric phase

4.1 Signal formulation

Assuming that the transmitted signal is a chirp:

$$p(t)=\mathrm{rect}(t/T_\mathrm{r})\exp(-\mathrm{j}\pi k_\mathrm{r}t^2), \tag{10}$$

where t indicates the range time (fast time), T_r is the pulse duration, and k_r is the chirp rate. Following conventional SAR formation, the signal received by the radar on the geosynchronous orbit in the slow- and fast-time domains (θ, t) is given by

$$s(t,\theta)=k\int\left[g_\mathrm{a}(\boldsymbol{r}_\mathrm{p},\boldsymbol{r}_\mathrm{s})\rho(\boldsymbol{r}_\mathrm{p})p\left(t-\frac{2\left|\boldsymbol{r}_\mathrm{p}-\boldsymbol{r}_\mathrm{s}(\theta)\right|}{c}\right)\cdot\exp\left(-\mathrm{j}\frac{4\pi\left|\boldsymbol{r}_\mathrm{p}-\boldsymbol{r}_\mathrm{s}(\theta)\right|}{\lambda}\right)R_\mathrm{p}^{-4}\right]\mathrm{d}\boldsymbol{r}_\mathrm{p}, \tag{11}$$

where $\rho(\boldsymbol{r}_\mathrm{p})$ represents the complex backscatter of the target located at $\boldsymbol{r}_\mathrm{p}=(x_\mathrm{p}, y_\mathrm{p}, z_\mathrm{p})$, λ is the wavelength, $\boldsymbol{r}_\mathrm{s}$ is the radar position vector, $R_\mathrm{p}=|\boldsymbol{r}_\mathrm{p}-\boldsymbol{r}_\mathrm{s}|$ is the range from the radar to the target, $g_\mathrm{a}(\boldsymbol{r}_\mathrm{p}, \boldsymbol{r}_\mathrm{s})$ is the antenna gain function, k includes the remaining parameters of the radar equation, and the radar position vector is $\boldsymbol{r}_\mathrm{s}(\theta)=(X(\theta), Y(\theta), Z(\theta))$ where the symbols are from Eq. (3).

4.2 Effect of orbit errors on GEOCSAR imaging

Since the trajectory of GEOCSAR results in the formation of shift-varying signatures, the classical linear SAR imaging algorithms like range-Doppler (RD) and chirp scaling (CS) algorithms based on the characteristic of shift-invariant cannot be applied to handle GEOCSAR data (Cumming and Wong, 2005). The time domain approach such as the confocal CSAR imaging, correlation algorithm, back-projection method, and tomographic reconstruction can be used (Knaell and Cardillo, 1995; Ishimaru *et al.*, 1998; Chan *et al.*, 1999). In this study, the 3D space-time confocal imaging algorithm is employed in the derivation. The focusing algorithm correlates the received signal from t=0 to T with the reference signal at position $\boldsymbol{r}_0=(x_0, y_0, z_0)$ (Ishimaru *et al.*, 1998). The output is then

$$S_0=k\int_0^T\int\left[g_\mathrm{a}(\boldsymbol{r}_\mathrm{p},\boldsymbol{r}_\mathrm{s})\rho(\boldsymbol{r}_\mathrm{p})p\left(t-\frac{2R_\mathrm{p}}{c}\right)\cdot p^*\left(t-\frac{2R_0}{c}\right)\exp\left(-\mathrm{j}\frac{4\pi(R_\mathrm{p}-R_0)}{\lambda}\right)R_\mathrm{p}^{-4}\right]\mathrm{d}\boldsymbol{r}_\mathrm{p}\mathrm{d}t, \tag{12}$$

where $R_0=|\boldsymbol{r}_\mathrm{s}-\boldsymbol{r}_0|$. The geometry of GEOCSAR imaging using the confocal algorithm is shown in Fig. 3.

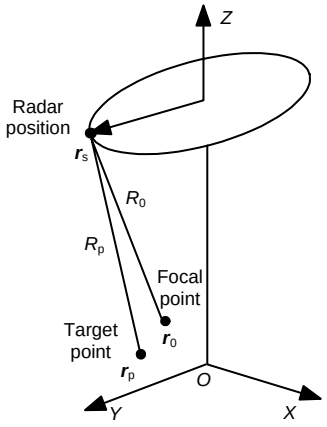

Fig. 3 Geometry of confocal geosynchronous circular synthetic aperture radar (GEOCSAR)

The integral

$$\int_0^T p(t-2R_\mathrm{p}/c)\,p^*(t-2R_0/c)\mathrm{d}t=g(R_\mathrm{p}-R_0)=\mathrm{sinc}\left(2B(R_\mathrm{p}-R_0)/c\right) \tag{13}$$

has a distinct peak for $R_\mathrm{p}=R_0$. The peak width defines the range resolution and is determined by the bandwidth B of the modulation function $p(t)$.

The SAR image formation is obtained by sampling S_0 over the SAR path, followed by coherent summation. Assuming the synthetic aperture of GEOCSAR in the θ domain is within (θ_s, θ_e), where θ_s represents the start aperture and θ_e represents the end aperture, the SAR signal S_p measured in the final processed image at position $\boldsymbol{r}_0$ may be represented as

$$S_\mathrm{p}=k\int_{\theta_\mathrm{s}}^{\theta_\mathrm{e}}\int\left[g_\mathrm{a}(\boldsymbol{r}_\mathrm{p},\boldsymbol{r}_\mathrm{s})\rho(\boldsymbol{r}_\mathrm{p}-\boldsymbol{r}_0)g(R_\mathrm{p}-R_0)\cdot\exp\left(-\mathrm{j}\frac{4\pi(R_\mathrm{p}-R_0)}{\lambda}\right)R_\mathrm{p}^{-4}\right]\mathrm{d}\boldsymbol{r}_\mathrm{p}\mathrm{d}\theta. \tag{14}$$

For a single point reflector at $\boldsymbol{r}_\mathrm{p}$, the SAR signal is

$$S(\boldsymbol{r}_\mathrm{p},\boldsymbol{r}_0)=k\int_{\theta_\mathrm{s}}^{\theta_\mathrm{e}}\Big[g_\mathrm{a}(\boldsymbol{r}_\mathrm{p},\boldsymbol{r}_\mathrm{s})\rho(\boldsymbol{r}_\mathrm{p}-\boldsymbol{r}_0)g(R_\mathrm{p}-R_0)\cdot\exp\left(-\mathrm{j}\frac{4\pi(R_\mathrm{p}-R_0)}{\lambda}\right)R_\mathrm{p}^{-4}\Big]\mathrm{d}\theta. \tag{15}$$

By varying $\boldsymbol{r}_\mathrm{p}$ around $\boldsymbol{r}_0$, the resolution function $G(\boldsymbol{r}_\mathrm{p},\boldsymbol{r}_0)=\left|S(\boldsymbol{r}_\mathrm{p},\boldsymbol{r}_0)\right|^2\Big/\left|S(\boldsymbol{r}_0,\boldsymbol{r}_0)\right|^2$ is mapped in all the three dimensions. In the range direction, the modulation bandwidth defines the resolution. In the cross-range plane, the 2D resolution will be determined by the synthetic aperture of GEOCSAR.

Assuming that the focal point and its close neighborhood are within the antenna main beam during the whole SAR path, the influence of $g_\mathrm{a}(\boldsymbol{r}_\mathrm{p}, \boldsymbol{r}_\mathrm{s})$ can then be moved outside the integral and neglected. Additional, the R_p^{-4} changes little during the whole synthetic aperture, and the amplitude modulating term can be regarded as a constant during the imaging processing. Assuming $R_\mathrm{p}-R_0<<c/(2B)$, $g(R_\mathrm{p}-R_0)$ can also be moved outside the integral. Ignoring all the constant terms, Eq. (15) can be rewritten as

$$S=\int_{\theta_\mathrm{s}}^{\theta_\mathrm{e}}\exp\left(-\mathrm{j}\frac{4\pi(R_\mathrm{p}-R_0)}{\lambda}\right)\mathrm{d}\theta. \tag{16}$$

For conveniently observing the focusing signal of GEOCSAR, we make further progress:

$$\begin{aligned}R_\mathrm{p}-R_0&=\left|\boldsymbol{r}_\mathrm{s}-\boldsymbol{r}_\mathrm{p}\right|-\left|\boldsymbol{r}_\mathrm{s}-\boldsymbol{r}_0\right|\\&\approx(\boldsymbol{r}_0-\boldsymbol{r}_\mathrm{p})\cdot(\boldsymbol{r}_\mathrm{s}-\boldsymbol{r}_0)\Big/\left|\boldsymbol{r}_\mathrm{s}-\boldsymbol{r}_0\right|\\&=\Big[(R_\mathrm{g}\cos\theta-x_0)\mathrm{d}x+(R_\mathrm{g}\sin\theta-y_0)\mathrm{d}y\\&+(A_a-0.5R_\mathrm{g}\cos\theta-\mathrm{z}_0)\mathrm{d}z\Big]\Big[(R_\mathrm{g}\cos\theta-x_0)^2\\&+(R_\mathrm{g}\sin\theta-y_0)^2+(A_\mathrm{a}-0.5R_\mathrm{g}\cos\theta-\mathrm{z}_0)^2\Big]^{-1/2},\end{aligned} \tag{17}$$

where A_a is the major semi-axis with no errors, $\mathrm{d}x=x_\mathrm{p}-x_0$, $\mathrm{d}y=y_\mathrm{p}-y_0$, $\mathrm{d}z=z_\mathrm{p}-z_0$, and the orbital elements are assumed to contain no errors. Since $i<<1$, then $R_\mathrm{g}=A_\mathrm{a}i<<A_\mathrm{a}$. Assuming $x_0<<A_\mathrm{a}$, $y_0<<A_\mathrm{a}$, we have

$$\begin{aligned}S&\approx\int_{\theta_\mathrm{s}}^{\theta_\mathrm{e}}\exp\left(-\mathrm{j}\frac{4\pi}{\lambda}(\boldsymbol{r}_0-\boldsymbol{r}_\mathrm{p})\cdot(\boldsymbol{r}_\mathrm{s}-\boldsymbol{r}_0)\Big/\left|\boldsymbol{r}_\mathrm{s}-\boldsymbol{r}_0\right|\right)\mathrm{d}\theta\\&\approx C_0\int_{\theta_\mathrm{s}}^{\theta_\mathrm{e}}\exp\left(-\mathrm{j}\frac{4\pi}{\lambda(A_a-\mathrm{z}_0)}\Big(R_\mathrm{g}\cos\theta(\mathrm{d}x-\mathrm{d}z/2)+R_\mathrm{g}\sin\theta\mathrm{d}y\Big)\right)\mathrm{d}\theta,\end{aligned} \tag{18}$$

where C_0 is a constant independent of θ. When the GEOCSAR imaging is made with full aperture measurement, i.e., $\theta_\mathrm{e}-\theta_\mathrm{s}=2\pi$, S can be expressed as

$$\begin{aligned}S&\approx C_0\int_{-\pi}^{\pi}\exp\left(-\mathrm{j}\frac{4\pi}{\lambda(A_\mathrm{a}-\mathrm{z}_0)}R_\mathrm{g}\mathrm{d}p\cos(\theta-\vartheta)\right)\mathrm{d}\theta\\&=C_0J_0\left(\frac{4\pi}{\lambda}\cdot\frac{R_\mathrm{g}\mathrm{d}p}{A_\mathrm{a}-\mathrm{z}_0}\right),\end{aligned} \tag{19}$$

where

$$\mathrm{d}p=\sqrt{(\mathrm{d}x-\mathrm{d}z/2)^2+(\mathrm{d}y)^2},\ \vartheta=\arctan\left(\frac{\mathrm{d}y}{\mathrm{d}x-\mathrm{d}z/2}\right),$$

and $J_0(x)$ is the Bessel function of zero order. Eq. (19) indicates that the resolution function of GEOCSAR with full aperture measurement is a Bessel function of zero order. Noting that the first zero of $J_0(x)$ is approximately at x=2.4, and considering its symmetry, we obtain the resolution as follows:

$$\Delta p=\frac{4.8\lambda(A-\mathrm{z}_0)}{4\pi R_\mathrm{g}}. \tag{20}$$

When the orbit has the error of $\delta\boldsymbol{r}_\mathrm{s}=(\Delta X, \Delta Y, \Delta Z)$, Eq. (18) becomes

$$\begin{aligned}S_\mathrm{e}&\approx\int_{\theta_\mathrm{s}}^{\theta_\mathrm{e}}\exp\left(-\mathrm{j}\frac{4\pi}{\lambda}(\boldsymbol{r}_0-\boldsymbol{r}_\mathrm{p}-\delta\boldsymbol{r}_\mathrm{s})\cdot(\boldsymbol{r}_\mathrm{s}-\boldsymbol{r}_0)\Big/\left|\boldsymbol{r}_\mathrm{s}-\boldsymbol{r}_0\right|\right)\mathrm{d}\theta\\&=\int_{\theta_\mathrm{s}}^{\theta_\mathrm{e}}\Big[\exp\left(-\mathrm{j}\frac{4\pi}{\lambda}(\boldsymbol{r}_0-\boldsymbol{r}_p)\cdot(\boldsymbol{r}_\mathrm{s}-\boldsymbol{r}_0)\Big/\left|\boldsymbol{r}_\mathrm{s}-\boldsymbol{r}_0\right|\right)\\&\cdot\exp\left(\mathrm{j}\frac{4\pi}{\lambda}\delta\boldsymbol{r}_\mathrm{s}\cdot(\boldsymbol{r}_\mathrm{s}-\boldsymbol{r}_0)\Big/\left|\boldsymbol{r}_\mathrm{s}-\boldsymbol{r}_0\right|\right)\Big]\mathrm{d}\theta\\&=C_0\int_{\theta_\mathrm{s}}^{\theta_\mathrm{e}}\Big[\exp\left(-\mathrm{j}\frac{4\pi R_\mathrm{g}\cdot\mathrm{d}p}{\lambda(A_\mathrm{a}-\mathrm{z}_0)}\cos(\theta-\vartheta)\right)\\&\cdot\exp\left(\mathrm{j}\frac{4\pi\left(R_\mathrm{g}\cos\theta(\Delta X-0.5\Delta Z)+R_\mathrm{g}\sin\theta\Delta Y\right)}{\lambda(A_\mathrm{a}-\mathrm{z}_0)}\right)\Big]\mathrm{d}\theta.\end{aligned} \tag{21}$$

Still take $\theta_\mathrm{e}=\pi$, $\theta_\mathrm{s}=-\pi$ for example. Because ΔX, ΔY, and ΔZ are sums of a series of cosine functions shown in Eq. (9), Eq. (21) can be expressed as

$$S_e \approx C_e \int_{-\pi}^{\pi} \left\{ \left[J_0\left(\frac{4\pi R_g \cdot dp}{\lambda(A_a - z_0)}\right) + 2\sum_{k=1}^{\infty} j^k J_k\left(\frac{4\pi R_g \cdot dp}{\lambda(A_a - z_0)}\right) \cdot \cos\left(k(\theta - \vartheta)\right) \right] \left[J_0\left(\frac{4\pi}{\lambda} a_1\right) + 2\sum_{k=1}^{\infty} j^k J_k\left(\frac{4\pi}{\lambda} a_1\right) \cdot \cos\left(k(2\theta - \beta_1)\right) \right] \left[J_0\left(\frac{4\pi}{\lambda} a_2\right) + 2\sum_{k=1}^{\infty} j^k J_k\left(\frac{4\pi}{\lambda} a_2\right) \cdot \cos\left(k(3\theta - \beta_2)\right) \right] \ldots \right\} d\theta, \quad (22)$$

where C_e is the constant term independent of θ, a_1, a_2 are the constant coefficients computed from the insertion of Eq. (9) into Eq. (21), and β_1, β_2 are the corresponding phases after a series of mathematical computations.

The integral result of Eq. (22) will be approximately expressed as

$$S_e \approx C_1 J_0\left(\frac{4\pi R_g \cdot dp}{\lambda(A_a - z_0)}\right) + C_2 J_2\left(\frac{4\pi R_g \cdot dp}{\lambda(A_a - z_0)}\right) + C_3 J_3\left(\frac{4\pi R_g \cdot dp}{\lambda(A_a - z_0)}\right) + \ldots, \quad (23)$$

where C_1, C_2, and C_3 are constant coefficients. Additionally, from the Bessel functions (Fig. 4) we can see that $J_k(x)$ attenuates with the increase of k. Thus, from Eq. (23) and Fig. 4 it can be seen that the mainlobe of the resolution function will be affected little, but the sidelobes will be severely influenced; i.e., the focusing quality like the peak sidelobe ratio (PSLR) and the integrated sidelobe ratio (ISLR) will be deteriorated. However, with the increase of orbital errors, the Bessel function of other orders (Fig. 2) may contribute more than that of the zero order to the SAR signal ($|C_2|$, $|C_3| >> |C_1|$), the mainlobe may be affected, and the output signal may even become unfocused.

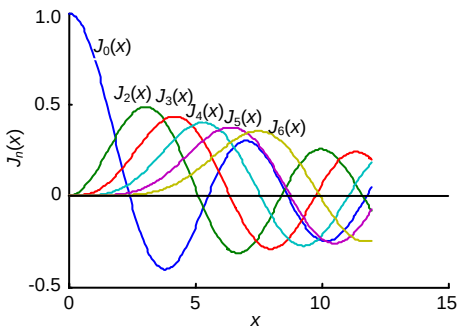

Fig. 4 Bessel function of several orders

4.3 Effect of orbit errors on GEOCSAR interferometric processing

The circular SAR configuration can produce the true 3D reconstruction by obtaining measurements made from several different azimuthal angles along the flight track. From Eqs. (13) and (20) we note that the range resolution comes primarily from the bandwidth, while the cross-range resolution depends mostly on the wavelength:

$$\Delta p = \frac{1.2\lambda(A - z_0)}{\pi R_g}, \quad \Delta r = \frac{c}{2B}, \quad (24)$$

where Δp indicates the 2D cross-range resolution of the target p, z_0 is the height of p, and Δr represents the range resolution.

Since GEOCSAR can produce high resolution true 3D images, it is favorable to estimate the surface deformation using GEOCSAR interferometry. First of all, the temporal decorrelation will be decreased in the interferometric GEOCSAR system for the one day revisit time (Madsen *et al*., 2001; Bruno *et al*., 2006). Second, the high 3D spatial resolution can be achieved for circular SAR imaging (Ishimaru *et al*., 1998; Axelsson, 2004). In conventional interferometry, the acquisition of the topography depends on the baseline, and the displacement is obtained by differentiating the 2D image pairs (subtracting the topography); hence, the baseline greatly influences the accuracy of the displament measurement. For surface displacement measurement of GEOCSAR interferometry, the interferogram can be produced directly from the high resolution 3D image pairs, and the effect of the baseline error propagating on the displacement error will be decreased. Besides, a GEOCSAR can provide a unique large coverage and continuous 24-h measurement of the target area, and these will benefit the disaster management (Madsen *et al*., 2001). Moreover, areas within the coverage region can be mapped from different view directions, and a GEOCSAR interferometry can provide 3D displacement data.

The interferometric processing relates two registered signals S_1 and S_2 to the Hermitian product $S_1 S_2^*$:

$$S_{\mathrm{p}}=S_1S_2^*=\int_{\theta_{\mathrm{s}}}^{\theta_{\mathrm{e}}}\int_{\theta_{\mathrm{s}}}^{\theta_{\mathrm{e}}}\iint\left\{\left|g(R_{\mathrm{p}}-R_0)\right|^2\rho(\boldsymbol{r}_{\mathrm{p}}-\boldsymbol{r}_0)\right.$$
$$\cdot\rho^*(\boldsymbol{r}_{\mathrm{p}'}-\boldsymbol{r}_0)\exp\left(-\mathrm{j}\frac{4\pi}{\lambda}\left(\left|\boldsymbol{r}_{\mathrm{s}1}-\boldsymbol{r}_{\mathrm{p}}\right|-\left|\boldsymbol{r}_{\mathrm{s}1}-\boldsymbol{r}_0\right|\right)\right) \tag{25}$$
$$\left.\cdot\exp\left(\mathrm{j}\frac{4\pi}{\lambda}\left(\left|\boldsymbol{r}_{\mathrm{s}2}-\boldsymbol{r}_{\mathrm{p}'}-\Delta\boldsymbol{x}\right|-\left|\boldsymbol{r}_{\mathrm{s}2}-\boldsymbol{r}_0\right|\right)\right)\right\}\mathrm{d}\boldsymbol{r}_{\mathrm{p}}\mathrm{d}\boldsymbol{r}_{\mathrm{p}'}\mathrm{d}\theta_1\mathrm{d}\theta_2,$$

where $\Delta\boldsymbol{x}=(\Delta x, \Delta y, \Delta z)$ is the deformation vector, $\boldsymbol{r}_{\mathrm{p}}$ and $\boldsymbol{r}_{\mathrm{p}'}$ are close to $\boldsymbol{r}_0$ in the same resolution cell, and the size of deformation is far less than the size of a resolution cell.

The final signal is obtained from the summation taken over the interferometric looks. If the surface is assumed to consist of uniformly distributed and uncorrelated scattering centers, then

$$\left\langle\rho(r_{\mathrm{p}})\rho^*(r_{\mathrm{p}'})\right\rangle=\sigma^0\delta(r_{\mathrm{p}}-r_{\mathrm{p}'}), \tag{26}$$

where σ^0 is the average radar cross section and '$\langle\cdot\rangle$' denotes ensemble averaging. Hence, Eq. (25) reduces to

$$S_{\mathrm{p}}=\left\langle S_{\mathrm{p}1}S_{\mathrm{p}2}^*\right\rangle=\int_{\theta_{\mathrm{s}}}^{\theta_{\mathrm{e}}}\int_{\theta_{\mathrm{s}}}^{\theta_{\mathrm{e}}}\int\left\{\sigma^0\left|g(R_{\mathrm{p}}-R_0)\right|^2\right.$$
$$\cdot\exp\left(-\mathrm{j}\frac{4\pi}{\lambda}\left(\left|\boldsymbol{r}_{\mathrm{s}1}-\boldsymbol{r}_{\mathrm{p}}\right|-\left|\boldsymbol{r}_{\mathrm{s}1}-\boldsymbol{r}_0\right|\right)\right) \tag{27}$$
$$\left.\cdot\exp\left(\mathrm{j}\frac{4\pi}{\lambda}\left(\left|\boldsymbol{r}_{\mathrm{s}2}-\boldsymbol{r}_{\mathrm{p}}-\Delta\boldsymbol{x}\right|-\left|\boldsymbol{r}_{\mathrm{s}2}-\boldsymbol{r}_0\right|\right)\right)\right\}\mathrm{d}\boldsymbol{r}_{\mathrm{p}}\mathrm{d}\theta_1\mathrm{d}\theta_2.$$

Making approximations using Eq. (17), Eq. (27) becomes

$$S_{\mathrm{p}}=\int_{\theta_{\mathrm{s}}}^{\theta_{\mathrm{e}}}\int_{\theta_{\mathrm{s}}}^{\theta_{\mathrm{e}}}\int\left\{\sigma^0\left|g(R_{\mathrm{p}}-R_0)\right|^2\right.$$
$$\cdot\exp\left\{-\mathrm{j}\frac{4\pi}{\lambda}\left[\left(\frac{\boldsymbol{r}_{\mathrm{s}1}-\boldsymbol{r}_0}{\left|\boldsymbol{r}_{\mathrm{s}1}-\boldsymbol{r}_0\right|}-\frac{\boldsymbol{r}_{\mathrm{s}2}-\boldsymbol{r}_0}{\left|\boldsymbol{r}_{\mathrm{s}2}-\boldsymbol{r}_0\right|}\right)(\boldsymbol{r}_0-\boldsymbol{r}_{\mathrm{p}})\right.\right. \tag{28}$$
$$\left.\left.\left.+\frac{\Delta\boldsymbol{x}\cdot(\boldsymbol{r}_{\mathrm{s}2}-\boldsymbol{r}_0)}{\left|\boldsymbol{r}_{\mathrm{s}2}-\boldsymbol{r}_0\right|}\right]\right\}\right\}\mathrm{d}\boldsymbol{r}_{\mathrm{p}}\mathrm{d}\theta_1\mathrm{d}\theta_2,$$

where the signal of the first exponent term represents the decorrelation signal, and the error due to topography information propagating into deformation is included. The signal of the second exponent term represents the interferometric signal with respect to the surface deformation, which needs to be resolved.

If the orbits have the errors of $\Delta\boldsymbol{r}_{\mathrm{s}1}$, $\Delta\boldsymbol{r}_{\mathrm{s}2}$, the interferometric signal from Eq. (28) can be expressed as

$$S_{\mathrm{pe}}=\int_{\theta_{\mathrm{s}}}^{\theta_{\mathrm{e}}}\int_{\theta_{\mathrm{s}}}^{\theta_{\mathrm{e}}}\int\left\{\sigma^0\left|g(R_{\mathrm{p}}-R_0)\right|^2\right.$$
$$\cdot\exp\left\{-\mathrm{j}\frac{4\pi}{\lambda}\left[\left(\frac{\boldsymbol{r}_{\mathrm{s}1}-\boldsymbol{r}_0}{\left|\boldsymbol{r}_{\mathrm{s}1}-\boldsymbol{r}_0\right|}-\frac{\boldsymbol{r}_{\mathrm{s}2}-\boldsymbol{r}_0}{\left|\boldsymbol{r}_{\mathrm{s}2}-\boldsymbol{r}_0\right|}\right)(\boldsymbol{r}_0-\boldsymbol{r}_{\mathrm{p}})\right.\right.$$
$$+\frac{\Delta\boldsymbol{x}\cdot(\boldsymbol{r}_{\mathrm{s}2}-\boldsymbol{r}_0)}{\left|\boldsymbol{r}_{\mathrm{s}2}-\boldsymbol{r}_0\right|}+\frac{\Delta\boldsymbol{r}_{\mathrm{s}1}\cdot(\boldsymbol{r}_{\mathrm{s}1}-\boldsymbol{r}_0)}{\left|\boldsymbol{r}_{\mathrm{s}1}-\boldsymbol{r}_0\right|} \tag{29}$$
$$\left.\left.\left.-\frac{\Delta\boldsymbol{r}_{\mathrm{s}2}\cdot(\boldsymbol{r}_{\mathrm{s}2}-\boldsymbol{r}_0)}{\left|\boldsymbol{r}_{\mathrm{s}2}-\boldsymbol{r}_0\right|}\right]\right\}\right\}\mathrm{d}\boldsymbol{r}_{\mathrm{p}}\mathrm{d}\theta_1\mathrm{d}\theta_2.$$

The interferometric phase signal for a single point target caused by the orbital errors is

$$S_{\mathrm{pe\_orbit}}=\int_{\theta_{\mathrm{s}}}^{\theta_{\mathrm{e}}}\int_{\theta_{\mathrm{s}}}^{\theta_{\mathrm{e}}}\exp\left[-\mathrm{j}\frac{4\pi}{\lambda}\left(\frac{\Delta\boldsymbol{r}_{\mathrm{s}1}\cdot(\boldsymbol{r}_{\mathrm{s}1}-\boldsymbol{r}_0)}{\left|\boldsymbol{r}_{\mathrm{s}1}-\boldsymbol{r}_0\right|}\right.\right.$$
$$\left.\left.-\frac{\Delta\boldsymbol{r}_{\mathrm{s}2}\cdot(\boldsymbol{r}_{\mathrm{s}2}-\boldsymbol{r}_0)}{\left|\boldsymbol{r}_{\mathrm{s}2}-\boldsymbol{r}_0\right|}\right)\right]\mathrm{d}\theta_1\mathrm{d}\theta_2$$
$$=\int_{\theta_{\mathrm{s}1}}^{\theta_{\mathrm{e}1}}\exp\left(-\mathrm{j}\frac{4\pi}{\lambda}\frac{\Delta\boldsymbol{r}_{\mathrm{s}1}\cdot(\boldsymbol{r}_{\mathrm{s}1}-\boldsymbol{r}_0)}{\left|\boldsymbol{r}_{\mathrm{s}1}-\boldsymbol{r}_0\right|}\right)\mathrm{d}\theta_1 \tag{30}$$
$$\cdot\int_{\theta_{\mathrm{s}2}}^{\theta_{\mathrm{e}2}}\exp\left(\mathrm{j}\frac{4\pi}{\lambda}\frac{\Delta\boldsymbol{r}_{\mathrm{s}2}\cdot(\boldsymbol{r}_{\mathrm{s}2}-\boldsymbol{r}_0)}{\left|\boldsymbol{r}_{\mathrm{s}2}-\boldsymbol{r}_0\right|}\right)\mathrm{d}\theta_2.$$

For full aperture measurement, the integral result of Eq. (30) can be analogously obtained from Eqs. (21) and (22). The result in Eq. (23) indicates that the sidelobes of the reconstructed image will be severely affected; hence, the interferometric processing of the two images will bring high noise in the interogram. These high noises can contaminate the phase observations significantly, resulting in an erroneous interpretation of the phase values. Besides the high noise from the affected sidelobes, the orbital errors may create improper interferometric phases. The interferometric phase for a single point caused by the orbital errors can be obtained from Eq. (22):

$$\Phi_{\mathrm{orbit}}=P\left\{C_{\mathrm{e}1}C_{\mathrm{e}2}^*\right\}, \tag{31}$$

where $P\{x\}$ represents extracting phase from x, C_{e} is as defined in Eq. (22), and subscripts 1 and 2 denote

the first and second images during interferometric processing respectively. If the radar carrier frequency is 1.25 GHz, the orbit error of 2.5 mm in *z*-direction would produce an approximately 0.12 rad phase.

From Eq. (29) we can also obtain the interferometric phase signal with respect to the deformation:

$$S_{\mathrm{pp}}=\int_{\theta_{\mathrm{s}}}^{\theta_{\mathrm{e}}}\exp\left(-\mathrm{j}\frac{4\pi}{\lambda}\Delta\boldsymbol{x}\cdot(\boldsymbol{r}_{\mathrm{s}2}-\boldsymbol{r}_0)\Big/\left|\boldsymbol{r}_{\mathrm{s}2}-\boldsymbol{r}_0\right|\right)\mathrm{d}\theta. \quad (32)$$

Comparing Eqs. (30) and (32), we can see that the sensitivities of the interferometric phase to the orbit errors and to the deformation will be on the same order. Therefore, the precise determination of an orbit would be one important influencing factor for accurate deformation measurement.

For surface deformation studies we wish to measure the three-component displacement in *x*-, *y*-, and *z*-direction. The interferometric phase varies with subaperture length and viewing angles. Thus, three interferometric observations from different subapertures of GEOCSAR are necessary to fully resolve the displacement field. Making further processing to the deformation phase in Eq. (32), we can conclude that the sensitivities of the phase to the displacements in *x*-, *y*-, and *z*-direction are on the order of

$$\begin{cases}\dfrac{\partial\phi}{\partial(\Delta x)}=\dfrac{4\pi(R_{\mathrm{g}}-x_0)}{\lambda R_0},\\[2ex] \dfrac{\partial\phi}{\partial(\Delta y)}=\dfrac{4\pi(R_{\mathrm{g}}-y_0)}{\lambda R_0},\\[2ex] \dfrac{\partial\phi}{\partial(\Delta z)}=\dfrac{4\pi(H-z_0)}{\lambda R_0}.\end{cases} \quad (33)$$

Since H is far larger than R_{g}, the interferometric phase is most sensitive to the height movement. Additionally, the sensitivity of the phase to the orbital error vector is

$$\frac{\partial\phi}{\partial(\Delta\boldsymbol{r})}=\frac{4\pi(\boldsymbol{r}_{\mathrm{s}}-\boldsymbol{r}_0)}{\lambda\left|\boldsymbol{r}_{\mathrm{s}}-\boldsymbol{r}_0\right|}, \quad (34)$$

where $\Delta\boldsymbol{r}$ is the orbital error vector. Comparing Eqs. (33) and (34), we can obtain the sensitivities of the displacement measurement to the orbital error:

$$\begin{cases}\dfrac{\partial(\Delta x)}{\partial(\Delta\boldsymbol{r})}=\dfrac{(R_{\mathrm{g}}-x_0)\left|\boldsymbol{r}_{\mathrm{s}}-\boldsymbol{r}_0\right|}{R_0(\boldsymbol{r}_{\mathrm{s}}-\boldsymbol{r}_0)},\\[2ex] \dfrac{\partial(\Delta y)}{\partial(\Delta\boldsymbol{r})}=\dfrac{(R_{\mathrm{g}}-y_0)\left|\boldsymbol{r}_{\mathrm{s}}-\boldsymbol{r}_0\right|}{R_0(\boldsymbol{r}_{\mathrm{s}}-\boldsymbol{r}_0)},\\[2ex] \dfrac{\partial(\Delta z)}{\partial(\Delta\boldsymbol{r})}=\dfrac{(H-z_0)\left|\boldsymbol{r}_{\mathrm{s}}-\boldsymbol{r}_0\right|}{R_0(\boldsymbol{r}_{\mathrm{s}}-\boldsymbol{r}_0)}.\end{cases} \quad (35)$$

It is noted from Eq. (35) that the sensitivity of the displacement measurement to the orbit error is greater in *z*-direction than in *x*- and *y*-direction.

5 Simulations

To illuminate the effects of orbit errors on GEOCSAR imaging and interferometric processing, several simulations have been carried out. Fig. 5 is a simulated ellipse satellite track with an orbit inclination (*i*) of 3°, an orbit eccentricity (*e*) of 0.026, and an argument of perigee of 90°. The track of the satellite path projected on the *XY* plane (subsatellite track) is a circle (Fig. 5b). The carrier frequency selection of the GEOCSAR system is set to be L-band, and the *XY* plane resolution cell for full aperture imaging is a circle with a radius of 2 m. For gaining likewise high height resolution, the bandwidth is set to be 100 MHz in the simulations (the bandwidth is ambitious in practice, and 30 MHz bandwidth may be more appropriate for the L-band SAR system). With the simulation parameters, the resolution on the *Z*-axis is approximately 2 m.

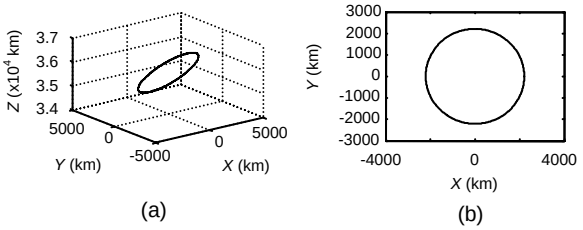

Fig. 5 Satellite track in the 3D space (a) and subsatellite track on the *XY* plane (b) at an orbit inclination of 3°, an orbit eccentricity of 0.026, and an argument of perigee of 90°

The confocal imaging algorithm is used to simulate the target located at (r_{t}, 0, $\sqrt{R_{\mathrm{e}}^2-r_{\mathrm{t}}^2}$), where r_{t}=1000 km and R_{e} is the radius of the Earth. The 2D point spread functions (PSF) of the *XY* plane with and

without orbit errors are shown in Fig. 6. From Eqs. (8) and (9) it can be seen that the orbit errors in X-, Y-, and Z-direction are of the form of $\sum_{n=2}^{\infty} a_n \cos(n\theta + \vartheta_n)$. Since the cosine terms of n>6 in Eq. (8) contribute little, we usually consider the terms of $n \leq 6$. In the simulations, the orbit errors in X-, Y-, and Z-direction are produced using

$$\begin{cases} \Delta X = \sum_{n=2}^{6} a_n \cos(n\theta + \varepsilon_n), \\ \Delta Y = \sum_{n=2}^{6} b_n \cos(n\theta + \varepsilon_n), \\ \Delta Z = \dfrac{\Delta X}{2}, \end{cases} \tag{36}$$

where a_n, b_n, and ε_n are random numbers. The standard deviations of ΔX, ΔY are assumed almost the same. The error values in the simulation figures all refer to the standard deviation of ΔX.

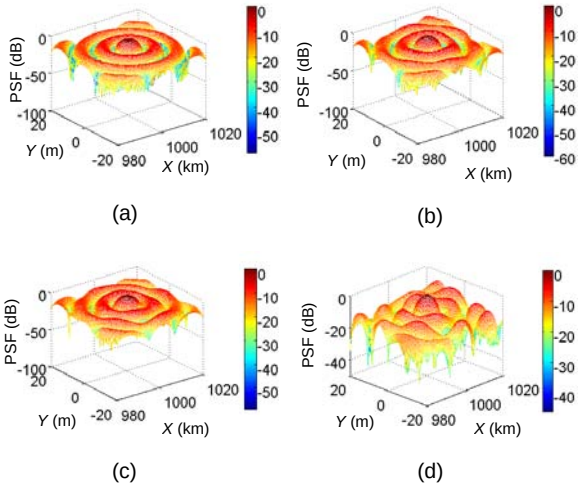

Fig. 6 Two-dimensional point spread functions without an error (a) and with an error of 10 mm (b), 20 mm (c), or 30 mm (d)

The focusing qualities in X- and Y-direction including PSLR and ISLR are compared in Table 1. The resolution cell in the XY plane is a circle for GEOCSAR imaging with full aperture measurement, and the focusing qualities in X- and Y-direction are the same. With the increase of the orbit error, the focusing qualities in the XY plane become inequable, and the PSLR and ISLR deteriorate. When the standard error is 30 mm, the PSLR and ISLR decrease by more than 1 dB. This means the orbit accuracy should be restricted within 30 mm.

Table 1 Focusing qualities comparison for four different orbit errors

	PSLR (dB)			
	0 mm	10 mm	20 mm	30 mm
X	−7.9051	−7.6266	−7.2953	−6.6130
Y	−7.9051	−7.8044	−7.4960	−7.0226
	ISLR (dB)			
	0 mm	10 mm	20 mm	30 mm
X	−4.7199	−4.4115	−4.1069	−3.5290
Y	−4.7199	−4.6331	−4.4954	−4.0450

PSLR: peak sidelobe ratio; ISLR: integrated sidelobe ratio

For conveniently observing the effect of orbit errors on the interferometric phase, first the deformation is set only in the height direction of a plane terrain Z=Z_0. The interferograms are obtained from the true 3D reconstruction images of GEOCSAR. In the simulations, the 2D interferograms are presented on the Z=Z_0 plane, extracted from the 3D interferograms. Fig. 7 illustrates the height deformation. Fig. 8 shows the corresponding deformation interferograms without and with orbit errors.

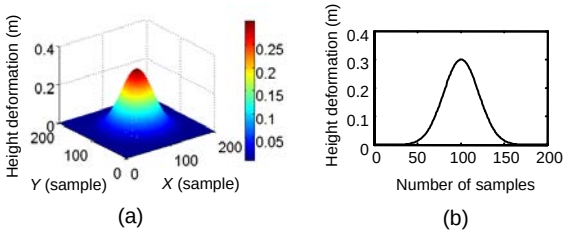

Fig. 7 Simulated height deformation

(a) 3D height deformation; (b) 2D height deformation projected on the X=Y plane

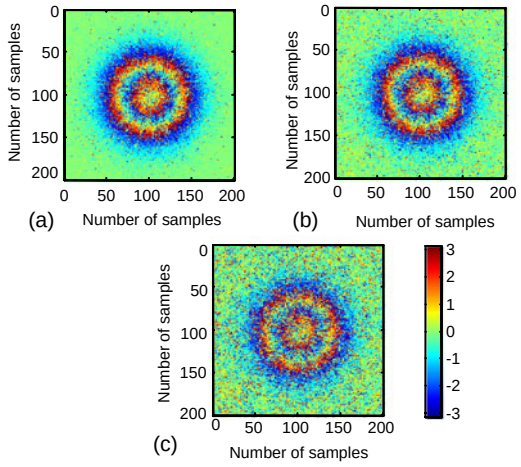

Fig. 8 Interferograms without an orbit error (a) and with an orbit error of 5 mm (b) or 10 mm (c)

With a standard error of 5 mm in radar positions, the interferometric fringes in Fig. 8b vary little, but more noise appears. When the error is increased to 10 mm, the noise increases severely and the interferometric fringes become obscured (Fig. 8c). The accuracies of the surface deformation obtained from these interferograms with orbit errors will decrease as well.

From the interferograms in Fig. 8, the deformation can be retrieved. Fig. 9 shows the retrieved deformation from interferograms without and with an orbit error. The original deformation is as shown in Fig. 7b. The statistical properties of the retrieval deformation results are presented in Table 2. Millimeter-scale accuracies of the deformation can be obtained from the interferograms without an orbit error or with a 5 mm error, while the accuracy is deteriorated to be centimeter-scale when the orbit error is increased to be 10 mm. Thus, it is indispensable to reduce the effects of the orbit error on the interferometric phase and to gain the precise surface deformation measurement.

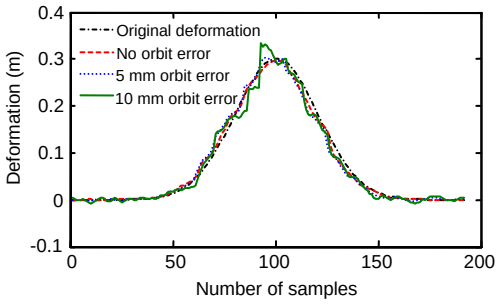

Fig. 9 Retrieved deformation from interferograms with and without an orbit error
The original deformation is as shown in Fig. 7b

Table 2 Standard deviations (SD) of deformation

	No orbit error	Orbit error 5 mm	Orbit error 10 mm
SD (m)	0.0037	0.0078	0.0149

An interferometric estimation of 3D surface deformation can be obtained using three or more geosynchronous subapertures. To estimate the three components of surface deformation, we begin by setting 3D deformation and obtaining the complex, single-look images with three subapertures of GEOCSAR. In the simulation, the subapertures setting is $(-\pi, -\pi/2)$, $(-\pi/3, \pi/6)$, $(\pi/3, 5\pi/6)$. For comparison, the interferograms are obtained from GEOCSAR subaperture processing with and without orbit errors. The corresponding retrieval deformations of three components are presented in Fig. 10.

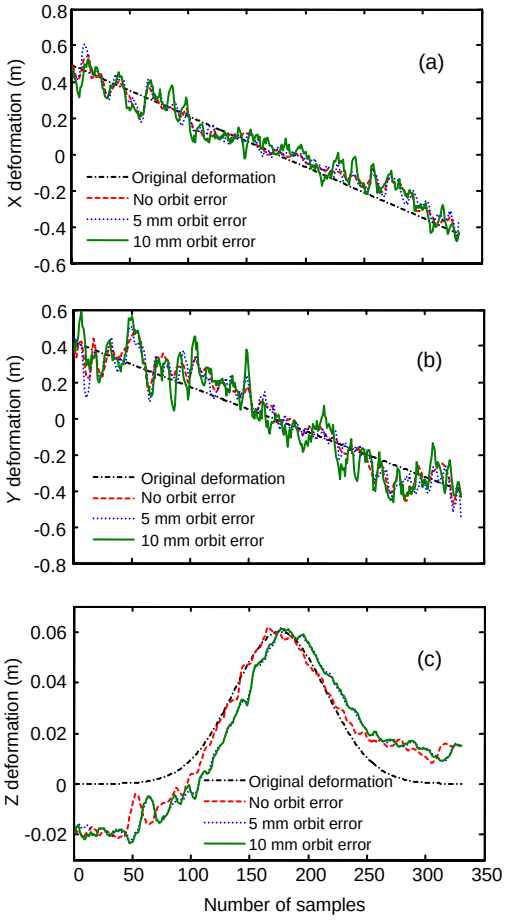

Fig. 10 Retrieved 3D deformations
(a) *X*-direction, (b) *Y*-direction, (c) *Z*-direction

Owing to the high sidelobe of GEOCSAR and numerical approximations of the retrieval equations, there are still errors for the retrieved deformations when no error is added. The standard deviations of the retrieval results are shown in Table 3.

Table 3 Standard deviations of deformation in *X*-, *Y*-, and *Z*-direction

	Standard deviation (m)		
	No orbit error	Orbit error 5 mm	Orbit error 10 mm
X	0.0320	0.0594	0.0968
Y	0.0562	0.0983	0.1494
Z	0.0077	0.0106	0.0118

The deformation accuracies show about threefold deterioration in *X*- and *Y*-direction and less than twofold deterioration in *Z*-direction, when the orbit error becomes 10 mm. The effect of orbit errors on deformation is more severe in *X*- and *Y*-direction than in *Z*-direction, which agrees with the theoretical analyses above. Since the orbit error of 10 mm greatly reduces the accuracies of deformations, the orbit error should be constrained to a few millimeters.

For GEOCSAR imaging interferometric processing, another important influencing factor is the atmospheric noise effect, which may seriously degrade the measuring accuracy and the imaging performance. The characterization of propagation effects introduced by the troposphere and ionosphere, and how to mitigate the atmospheric effects are the future work.

6 Conclusions

GEOCSAR is an innovative SAR system, which not only is able to obtain high resolution 3D images and offer continuous surveillance for a broad area, but also has the potential to make high resolution 3D deformation measurement. Since the orbit of GEOCSAR is very high, the dynamical effects on the orbit behave much different from the conventional low orbit spaceborne SAR. The main factors influencing orbit motions are the perturbing effects and the difference between the designed orbital elements and the geostationary orbital element. Thus, the orbit estimation should consider the contributions of both perturbations and the designed orbital elements, and the orbit errors will depend on the accuracy of the orbit estimation. Effects of GEOCSAR orbit errors on final images and interferograms are qualitatively evaluated by theoretical analysis and quantitatively estimated by processing simulated raw data. The orbit errors affect the focusing quality like PSLR and ISLR of the GEOCSAR images, even making the images unfocused when the error increases. Simulations demonstrate that the relative precision of orbit during the integration time should be at the centimeter level for ensuring the image qualities. For deformation interferometric measurement, a relative orbit error of 10 mm will result in a deformation error of approximately several millimeters; hence, the orbit should be accurately estimated to decrease the effect. Moreover, the sensitivity of the orbit error to the deformation is greater in *X*- and *Y*-direction than in *Z*-direction. By theoretical analyses and simulations in this study, we conclude that the millimeter-scale relative orbit accuracy is required for GEOCSAR interferometric processing.

References

Axelsson, S.R.J., 2004. Beam characteristics of three-dimensional SAR in curved or random paths. *IEEE Trans. Geosci. Remote Sens.*, **42**(10):2324-2334. [doi:10.1109/TGRS.2004.834802]

Bruno, D., Hobbs, S.E., Ottavianelli, G., 2006. Geosynchronous synthetic aperture radar: concept design, properties and possible applications. *Acta Astronaut.*, **59**(1-5):149-156. [doi:10.1016/j.actaastro.2006.02.005]

Cantalloube, H.M.J., Colin-Koeniguer, É., Oriot, H., 2007. High Resolution SAR Imaging along Circular Trajectories. IGARSS, p.850-853. [doi:10.1109/IGARSS.2007.4422930]

Cassara, P.P., 1963. The Influence of Tesseral Harmonics and Lunisolar Gravitation on the Motion of a 24-Hour Satellite. AIAA, p.63-153.

Cazzani, L., Colesanti, C., Leva, D., Nesti, G., Prati, C., Rocca, F., Tarchi, D., 2000. A ground-based parasitic SAR experiment. *IEEE Trans. Geosci. Remote Sens.*, **38**(5):2132-2141. [doi:10.1109/36.868872]

Chan, T.K., Kuga, Y., Ishimaru, A., 1999. Experimental studies on circular SAR imaging in clutter using angular correction function technique. *IEEE Trans. Geosci. Remote Sens.*, **37**(5):2192-2197. [doi:10.1109/36.789616]

Colesanti, C., Perissin, D., 2006. A first experiment of 3D imaging with a ground based parasitic SAR. IGARSS, p.1192-1195. [doi:10.1109/IGARSS.2006.308]

Cumming, I.G., Wong, F.H., 2005. Digital Processing of Synthetic Aperture Radar Data: Algorithms and Implementation. Artech House, Inc., London, p.25-109.

Erik, M.S., 1994. Handbook of Geostationary Orbits (1st Ed.). Kluwer Academic Publishers, the Netherlands, p.886-1070.

Hanssen, R.F., 2002. Radar Interferometry—Data Interpretation and Error Analysis. Kluwer Academic Publishers, the Netherlands, p.42-155.

Ishimaru, A., Chan, T.K., Kuga, Y., 1998. An imaging technique using confocal circular synthetic aperture radar. *IEEE Trans. Geosci. Remote Sens.*, **36**(5):1524-1530. [doi:10.1109/36.718856]

Kimura, H., Todo, M., 1997. Baseline Estimation Using Ground Points for Interferometric SAR. IGARSS, p.442-444. [doi:10.1109/IGARSS.1997.615909]

Knaell, K.K., Cardillo, G.P., 1995. Radar tomography for the generation of three-dimensional images. *IEE Proc.-Radar Sonar Navig.*, **142**(2):54-60. [doi:10.1049/ip-rsn:19951791]

Li, F.K., Held, D.N., Curlander, J.C., Wu, C., 1985. Doppler parameter estimation for spaceborne synthetic aperture radars. *IEEE Trans. Geosci. Remote Sens. Lett.*, **23**(1):47-56. [doi:10.1109/TGRS.1985.289499]

Liu, J.Y., Zhu, J.B., Hu, Z.H., Liu, Y., 2006. Error compensation and high-precision baseline estimation in InSAR geolocation using GCPs. *SPIE*, **6418**:64180L. [doi:10.1117/12.712616]

Madsen, S.N., Edelstein, W., Didomenico, L.D., LaBrecque, J., 2001. A Geosynchronous Synthetic Aperture Radar: for Tectonic Mapping, Disaster Management and Measurements of Vegetation and Soil Moisture. IGARSS, p.447-449. [doi:10.1109/IGARSS.2001.976185]

Madsen, S.N., Chen, C., Edelstein, W., 2002. Radar Options for Global Earthquake Monitoring. IGARSS, p.1483-1485. [doi:10.1109/IGARSS.2002.1026156]

Musen, P., Bailie, A.E., 1962. On the motion of a 24-hour satellite. *J. Geophys. Res.*, **67**(3):1123-1132. [doi:10.1029/JZ067i003p01123]

NASA, 2003. Global Earthquake Satellite System: a 20-Year Plan to Enable Earthquake Prediction. Available from http://solidearth.jpl.nasa.gov/gess.html [Accessed on Sept. 28, 2009].

Ren, K., Prinet, V., Shi, X.Q., Wang, F., 2003. Comparison of Satellite Baseline Estimation Methods for Interferometry Applications. IGARSS, p.3821-3823. [doi:10.1109/IGARSS.2003.1295281]

Shrivastava, S.K., 1978. Orbital perturbations and station-keeping of communication satellites. *J. Spacecraft Rock.*, **15**(2):67-78. [doi:10.2514/3.27999]

Tomiyasu, K., 1978. Synthetic Aperture Radar in Geosynchronous Orbit. IEEE Antennas and Propagation Symp., p.42-45. [doi:10.1109/APS.1978.1147948]

Tomiyasu, K., 1983. Synthetic aperture radar imaging from an inclined geosynchronous orbit. *IEEE Trans. Geosci. Remote Sens.*, **21**(3):324-329. [doi:10.1109/TGRS.1983.350561]

Yoon, J.C., Lee, K.H., Lee, B.S., 2004. Geostationary orbit determination for time synchronization using analytical dynamic models. *IEEE Trans. Aerosp. Electron. Syst.*, **40**(4):1132-1146. [doi:10.1109/TAES.2004.1386869]

Zhang, J.X., Cao, X.B., 2004. Analysis and simulation of satellite system parameter effect on SAR Doppler parameters. *J. Electron. Inform. Technol.*, **26**(11):1746-1751 (in Chinese).

Zhang, L., Wu, J.C., Ding, X.L., Xiao, F., 2007. The Propagation of Orbital Errors in the 3-Pass DInSAR Processing. 1st Asian and Pacific Conf. on Synthetic Aperture Radar, p.550-554. [doi:10.1109/APSAR.2007.4418671]

Zhou, P., Pi, Y.M., Wang, J.F., 2007. Precise Computation of Doppler Parameters for Spaceborne SAR in Elliptic Orbits. IGARSS, p.721-724. [doi:10.1109/APSAR.2007.4418713]